E-ISSN: 2583-9667
Indexed Journal
Peer Reviewed Journal
https://multiresearchjournal.theviews.in

Received: 04-04-2024
Accepted: 16-06-2024

INTERNATIONAL JOURNAL OF ADVANCE RESEARCH IN MULTIDISCIPLINARY

Volume 2; Issue 3; 2024; Page No. 485-491

Diffractometer for x-rays, a microscope for transmission electron scattering (TEM), and Raman Spectroscopy

[1]Mugale Yogesh Gopal and [2]Dr. Suryawanshi Venkat S

[1]Research Scholar, Department of Chemistry, Shri Chhatrapati Shivaji College, Omerga, Osmanabad, Maharashtra, India
[2]Professor, Department of Chemistry, Shri Chhatrapati Shivaji College, Omerga, Osmanabad, Maharashtra, India

DOI: https://doi.org/10.5281/zenodo.14995298

Corresponding Author: Mugale Yogesh Gopal

Abstract

There is a great deal of curiosity about the physicochemical characteristics of tiny particles made of magnetic oxide in the chemical industry and in research into their potential applications in electronics, biomedicine, and environmental remediation, among many other areas. Magnetic oxide nanoparticles and chemical methods are used in this study to produce iron oxide ($FePO_4$ and -Fe_2O_n), with a focus on sol-gel synthesis and co-precipitation. The primary objective is to design chemically stable nanoparticles with controllable size, shape, style, and magnetic properties. Mechanical, chemical, and physical properties of the produced nanoparticles are studied by employing imaging techniques like scanning electron microscopy (SEM), vibrating sample magnetometry (VSM), and X-ray diffraction (XRD), among others. These include the nanoparticles' size, shape, surface charge, crystallinity, and magnetic behaviour. Additionally, the study delves into the process of surface functionalization and the ways in which response variable elements influence the degree of behaviour of the final nanoparticle.

The size and magnetic characteristics of the synthesized magnetic oxide nanoparticles may be adjusted by changing the synthesis conditions, and they display superparamagnetic behaviour. Thanks to their versatility, they may be used for a wide range of tasks, such as medication delivery, MRI scanning, and chemical processes. This study contributes to our understanding of how different synthesis methods affect the magnetic and chemical characteristics of nanoparticles, which may be used to better customize these materials for various technical and commercial uses.

Keywords: Raman spectroscopy; X-ray diffraction; scanning electron microscopy (SEM)

Introduction

Highly magnetic materials are not only poisonous but also easily oxidized like nickel and cobalt are not very useful. The increased larger surface areas, slower sedimentation rates, and an increase in the proportion of particles dispersed in tissue that are smaller than 100 nm constitutes the main advantages of their use. Because nanoparticles grow as r6, another benefit is a dramatic reduction in magnetic dipole-dipole interactions. To minimize vascular embolism in the biomedical usage of magnetic nanoparticles in living organisms requires their safety, non-toxic, and non-immunogenic. They also need to be small enough to circulate upon injection and traverse organ and tissue capillary networks. Additionally, they need to be highly magnetized so that a magnetic field can regulate their blood flow and immobilize them near the diseased tissue that has to be treated. Since there are less stringent size constraints in *in vitro* applications compared to uses in living organisms, composites with lengthy sedimentation periods of superparamagnetic nanocrystals distributed in submicron diamagnetic particles that do not need a magnetic field to function. Using diamagnetic matrices has the key advantage of being easy to functional preparation of the superparamagnetic composites.

The polymer takes on the characteristics of the hard clay nanoparticles. Smart and functional apparel has also been made possible by attaching nanoparticles to textile fibers. Nanoscale material differences affect features of electrons inside matter and interactions between atoms that are wave-like (quantum mechanical). What are the magnetic characteristics, melting point, charge capacity, and even color may be controlled by fabricating structures on the

nanoscale scale, all without altering the material's chemical makeup. Harnessing this potential will enable previously unimaginable innovations in high-performance goods and technology. The extraordinary feature ratios of when it comes to surface area to volume and aspect ratio, nanoscale structures like nanoparticles and nanolayers are very adaptable and can be incorporated into a variety of materials. Biosynthetic techniques, microemulsion include biological synthesis, spark discharge, template synthesis, inert gas condensation, sol-gel, sonochemistry, and hydrothermal synthesis, and pulse laser ablation are some of the ways that nanoparticles may be created. Now, let's take a quick look at the techniques used to synthesize nanoparticles.

Literature Review

Saviska Luqyana Fadia *et al*. (2024) [1] Analyzing and characterizing magnetic wood synthesized using magnetite nanoparticles in an ex-situ impregnation procedure was the goal of this investigation. The procedure began with the co-precipitation technique of synthesizing magnetite nanoparticles, and the nano-magnetite was successfully produced with particles ranging in size from 17 to 233 nanometres with an average size of 75 nanometres. Untreated and furfurylated wood were also included in magnetite nanoparticles in furfuryl alcohol at three distinct concentrations, in addition to the impregnation solution. As an additional option, the poor physical qualities of the wood from the *Falcataria moluccana* Miq. species was used. The samples were immersed in the solution during the impregnation procedure subjected to a pressure of 0.5 bar for half an hour, then 1 bar for two hours. Physical features including density, anti-swelling efficiency, weight % growth, and bulking impact all improved, while water uptake kept going down. Magnesite nanoparticles were also visible in the microstructure of the wood, which was corroborated by the determination of ferrum concentrations by chemical element analyses. Analyses of chemical changes demonstrated the existence of a cross-linked this wood polymer has an iron-oxygen functional group.

Ancuta Trifoi *et al*. (2023) [2] Reasons being, they are safe for the body, have less toxicity, and superparamagnetism, magnetite nanoparticles have piqued the attention of scientists in many disciplines, including chemistry, biology, physics, and medicine. Magnetic nanoparticles with precisely modulated size, shape, and magnetic characteristics may be synthesized using a number of different approaches. While there are a number of methods for producing nanoparticles, the most popular one is coprecipitation because to its cheap cost, simplicity, and environmentally benign reaction conditions; yet, it is not very reproducible.

S. Mangala Devi *et al*. (2019) [3] Nanoparticles of iron oxide: its characteristics and uses in the physical sciences, chemistry, and catalysis were examined in this paper's extensive literature study. Iron oxide's exceptional magnetic characteristic has led to its adaptable advancement in recent years. According to earlier studies that used Scherrer's formula, the typical size of a crystallite is between 10 and 45 nanometers. Researchers observed that the powder had a mostly spherical and intentionally quasi-spherical form. Using the N2 adsorption BET isotherm, the area of the given surface was determined to be between 17.6-26.21 m^2/g. A typical spinel structure or an inverted one might be obtained, based on the approach of synthesis. The magnitude of the crystallites was found to be between 8 and 42 nanometers, as shown by using Radiographic analysis using XRD.

Mohammad Moniruz Zaman *et al*. (2019) [4] Spinel magnetite nanoparticles (MNPs) made of Fe3O4 were effectively produced by reducing the stoichiometric use a NaOH solution in order to calculate the proportion of Fe^{2+} to Fe^{3+} in water. To modify the surface of MNPs, biomolecules from the naturally occurring there was a usage of an aqueous extract using the plant's extract from the leaves of the Ipomoea aquatica plant, which serves as a stabilizing agent. Investigations using gas chromatography mass spectrometry (GCMS), Biomolecules isolated from the leaf extract show promise Integrating energy dispersive X-ray (EDX) and Fourier transform infrared (FTIR) investigations into MNPs has been done adequately. Experimenting with X-ray diffraction (XRD) under a microscope verifies the uniform size distribution and spherical shape of the produced MNPs, while The production procedure is confirmed using transmission electron microscopy (TEM) and field emission scanning electron microscopy (FESEM).

Research Methodology

Diffractometer for X-rays

Critically important analytical tools is X-ray diffraction which is primarily implemented to gather structural information about the crystalline materials. It is used to collect information on unit cell dimension of the materials. To achieve electromagnetic diffraction, the separation between the gratings should be of the order of incident wavelength. For interplanar spacing of crystals, the separation is ~2-3 Å, which is suitable for XRD. X-rays, diffracted from the array of atoms of the crystals in specific directions and different intensities, provides a clear insight about the crystal structure including crystallite size, chemical bonding etc. The basic principle which is followed in determining the crystallographic parameters from procured XRD data is The formula for Bragg's law is $2d\sin\theta = n\lambda$, where d is an integer and λ is the wavelength. interplanar spacing of the atoms is denoted by θ). What follows is a diagram depicting Bragg's diffraction law. In our case prepared samples have been characterized by an advanced D8 diffractometer of Bruker, operating radiation Cu–Kα (λ= 1.5418 Å) with scan limit 10°- 80°. Determination of $D=k\lambda/\beta\cos\theta$, where K ~ 0.93-0.94, λ (wavelength) = 0.15418 nm for CuKα The crystallite's size (D) may be calculated using the variables β (full width at half maximum) and θ (diffraction angle). were used. In case of nominal substitution, to realize minor changes in grain sizes and lattice parameter of the samples, We used Rietveld refining on the XRD data that we acquired using MAUD software for analysis.

The FESEM, or scan electron microscope that uses field emission technology,

The surface topography of samples is often observed using FESEM. Strongly charged electrons kinetic energy emitted from an electron gun, are made to incident on the object. The scattered electrons ejected from the object under investigation are captured and an image is formed on the

screen. In our work, a FESEM instrument of Inspect –FEI, USA microscope was used. A schematic depicting the basic principle of FESEM is given below.

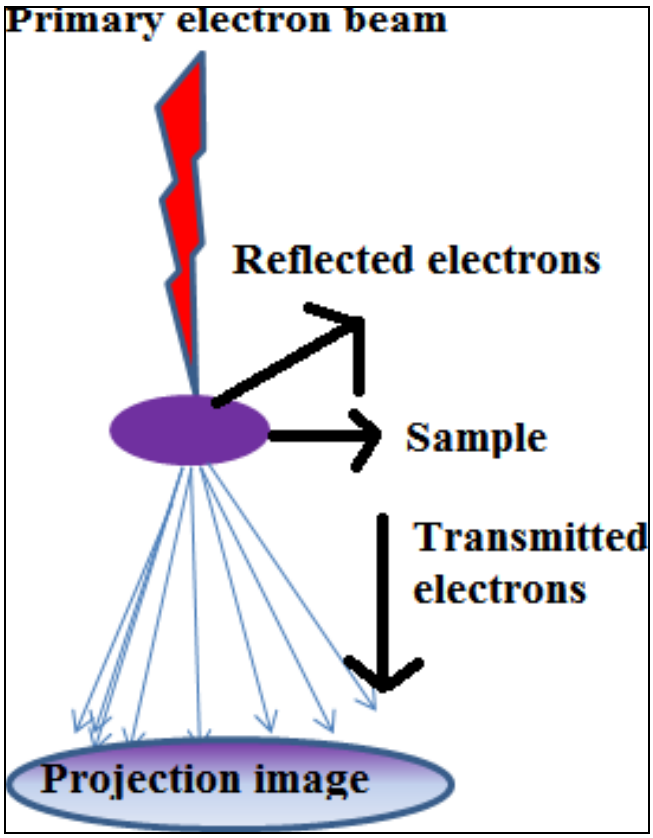

Fig 1: Schematic representation of basic principle of FESEM

Microscope for Transmission Electron Scattering (TEM)
Examination of the samples is carried out using the transmission electron microscope (TEM) morphology to a finer degree. A very energetic electron beam interacts with a very thin material. Using the specimen's transmitted electrons, a picture is created using an imaging device such as a photographic screen or sensors. TEM images with higher resolution than normal are also termed HRTEM pictures, which are high-resolution transmission electron micrographs. Imaging techniques such as HRTEM, SAED, and EDX patterns are often provided. Here we have used JEOL, JEM-2011 instrument for TEM.

Raman Spectroscopy
Researchers use Raman spectroscopy to learn more about distortion of lattice, structural transition, spin–lattice and lattice charge–lattice couplings, magnetic ordering and distribution of local cations, and of the materials. The basic principle behind fundamental to how Raman spectroscopy operates is the idea of inelastic monochromatic light scattering generally from a laser. Interaction of the laser with molecular vibrations or phonons within the molecule often consequence some laser photon shift. This shift gives a clear idea about the vibrational modes of the sample. LabRAM HR Raman spectrometer by Horiba was implemented for Raman spectra recording of the samples.

Spectroscopy that uses both visible and ultraviolet light
By using ultraviolet light spectroscopy, one may identify the materials' optical bandgap. Valence electrons of the outermost layer of valence band absorb light and gets excited to conduction band. That particular excitation wavelength resembles width of the material's band. Using Tauc plot, (αhν) = A (hν-Eg)n, hν be the incident energy, α, the coefficient of absorption, Where n is the number of nanometers in the band gap and Eg is a constant. = ½ or 2 for The band gap may be determined by calculating the materials' direct or indirect transitions. Across all available experiments here JASCO 530V UV-VIS spectrophotometer was used.

VSM measurements
This experiment measured the effects of an electromagnetic field between -10,000 and +10,000 Oe without chilling the samples using a vibrating sample magnetometer (VSM) of the PMC Micro Mag 3900 type, equipped with a 1 T magnet.

Analysis
Analyzing the structure
Nanohybrids of NZ and rGO were synthesized using a two-step procedure. The structural validity XRD results verified the quality of the manufactured samples. The XRD patterns seen in the NZ/rGO nanohybrid, the as-synthesized rGO sheet, and NZ are shown in Figure 3 (a-c), correspondingly. The unique peaks seen in the Analysis of NZ and NZ/rGO XRD patterns are attributed to cubic spinel ferrite. The (002) reflection typical of graphene is seen by the NZ/rGO and bare rGO peaks at 2θ = 26.22°. In contrast According to our earlier research, the aforementioned peak demonstrated that graphene exhibited a high degree of crystallinity. According to there is no restacking of rGO since No diffraction peak at 2θ= 25° is seen in the XRD patterns of the NZ/rGO nanohybrid and rGO. This outcome is anticipated because to the strong interfacial interaction that forms between the rGO surface and the NZ nanoparticles. There is a little shift in the diffraction peaks of the NZ/rGO sample when compared to pure NZ. The smooth merging of NZ with the rGO structure is seen here.

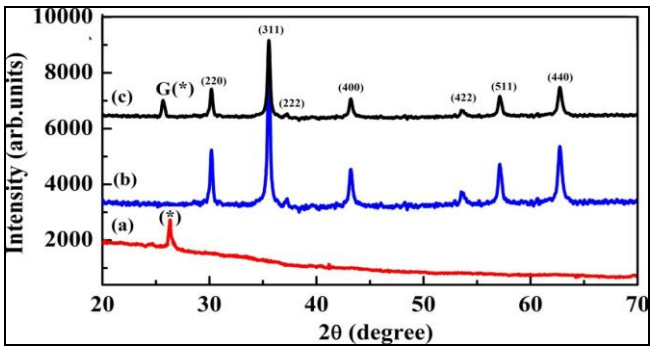

Fig 2: Structure of XRD reduced graphene oxide (c) zeolite, (b) reference gas, and zeolite/reduced graphene oxide (NZ/rGO) nanocomposite.

Morphological analysis
Figures 3 ((a), (c), and (e) show transmission electron micrographs of NZ, naked rGO, and nanohybrids of NZ and rGO, in that order. The shape of the NZ nanostructures produced by the sol-gel auto-combustion process is shown in Figure 3 (a). The typical size of the particles as measured

by TEM is about 20–35 nm. Due to elevated surface energy, inorganic nanomaterials synthesized via solution-based methods, such as sol-gel auto-combustion, exhibit a pronounced propensity into bigger, more amorphous structures to clump together. Pictured in A representative SAED from NZ is shown in Figure 3 (b). The design includes planes of reflection that align with the XRD results. Figure 3 (d) demonstrates that the majority of the NZ/rGO nano hybrids are evenly dispersed throughout the graphene surface, whereas a small number of being embedded within the two-dimensional matrix of rGO.

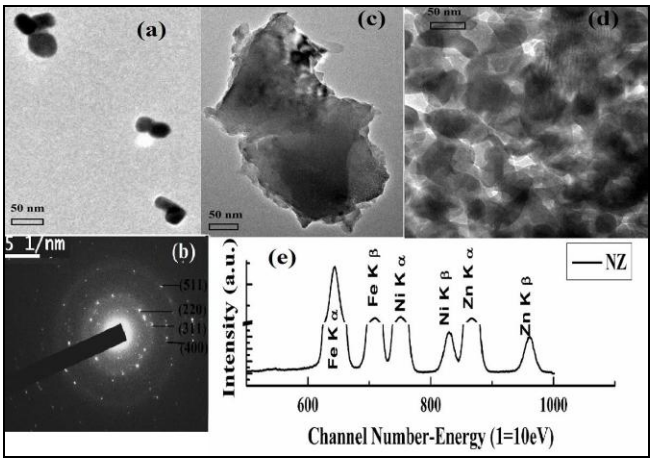

Fig 3: (a–c) By using transmission electron microscopy images of rGO and NZ; (b) secondary atomic emission spectra (SAED) of NZ; (d) secondary atomic imaging of the NZ/rGO nanocomposite; and (e) secondary atomic emission spectra (EDXRF) of NZ

This leads to the functionalisation of the rGO sheet, which in turn causes the rGO to exfoliate. The results show that the NZ composite was formed in the nano regime with the rGO sheet, as confirmed by the TEM pictures. The nano hybrid now has particles ranging in size from 40 to 45 nanometers. That being said, is no naked NZ or rGO further proves that the NZ nanoparticle and rGO matrix form a strong interfacial interaction. Figure 3 (e) Displays the EDS-XRF pattern, proving the sample's purity by showing in the NZ sample, which contains Ni, Zn, and Fe.

Table 1: Comparison of average XRD values for crystallite size and TEM values for particle size

Sample Code	Average crystallite size from XRD (nm)	Particle size from TEM (nm)
NZ	30	20-25
NZ/rGO	38	40-45

Using thermo gravimetric data

Here are the TGA curves of rGO, NZ, and the NZ/rGO nanohybrid: (a), (b), and (c), respectively, from Figure 4. As seen in Figure 4 (a), that rGO first lost 10% of its weight at temperatures lower than 350 °C. The breakdown of any remaining oxygen-containing functional groups might be a contributing factor. Afterwards, there was a decrease in weight between 350 and 750 degrees Celsius, which might be linked to the elimination of functional groups that contain stable oxygen. There were two main phases of NZ's weight reduction, as mentioned previously. At around 350 °C, the initial the water trapped in the lattice evaporates, causing weight loss and the disintegration of the citrate-nitrate precursor. Organic matter clearance was linked as 550 °C causes a second weight loss. Very little weight loss was seen when temperatures above 550 °C. As high as 600 degrees Celsius, the NZ/rGO nanohybrid maintained almost constant weight loss compared to pure rGO and NZ. Also, weight loss was very sluggish when temperatures above this. The result was a nanohybrid that was very stable throughout a broad temperature range. Regarding weight loss as a result of phase transitions, the graph does not show any sudden changes. The produced nanohybrid has a greater thermal stability compared to several of the ferrite/rGO nanocomposites that have been described before.

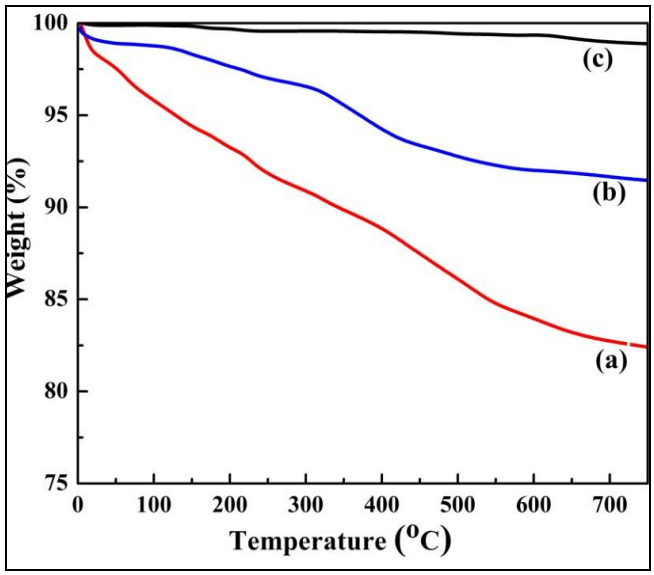

Fig 4: TGA plots of several nanocomposites: (a) NZ, (b) rGO, and (c) NZ/rGO.

The examination of Raman spectra

The degree of crystallization in rGO is often evaluated using Raman spectroscopy, which is considered a standard approach. Displayed in Figures 4-6 (a), (b) and (c) showcase the Raman spectra of rGO, NZ, and the NZ/rGO hybrid, respectively. nanocomposite, separately. Changes in the typical D and G bands, at 1345 cm^{-1} and 1595 cm^{-1}, respectively, as illustrated in Figure 4 (a), are caused by phonon vibrations, sp2 hybridized structural randomization, and graphene C-C stretching vibrations. The vibrational bands detected in pure NZ at 413 cm^{-1} and 651 cm^{-1} Figure 5(b)) show that the octahedral sublattice exhibits symmetric-asymmetric metal-oxygen bonds (Eg type), whereas the tetrahedral sublattice exhibits A1g type metal-oxygen vibrations. Figure 6(c) shows the nanohybrid's Raman spectra, which clearly show vibrational bands associated with graphene and ferrite. Possible correlation between composite creation and the observed change in the aforementioned band locations. The in-situ decrease of GO to rGO is confirmed by the fact that the ID/IG ratio (0.87) for The NZ/rGO nanohybrid exhibits an increase in rGO of 1.37. Expanding on our earlier research, this observation makes it abundantly evident that the nanohybrid is more disordered and has more surface flaws.

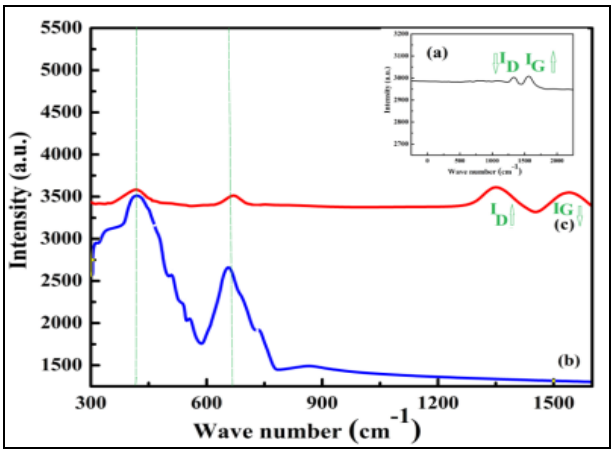

Fig 5: Reducing graphene oxide, NZ, and NZ/reduced graphene oxide were examined using Raman spectra nanocomposite.

Mössbauer analysis

Mössbauer technology serves as a crucial method for detecting Magnetic moments, cation distributions, with very delicate interactions in spinel ferrites. The NZ and NZ/rGO nanohybrid samples' room temperature Mössbauer spectra (in transmission mode) are shown in Figures 5 (a) and (b). Hyperfine splitting with a room temperature doublet in the spectra indicates an ordered state of the magnetic ions and specific relaxation phases associated with smaller particles. Table displays the hyperfine spectra-derived values of the isomer shift (I.S.), quadruple splitting (Q.S.), and magnetic hyperfine field (Hint) 4.1.

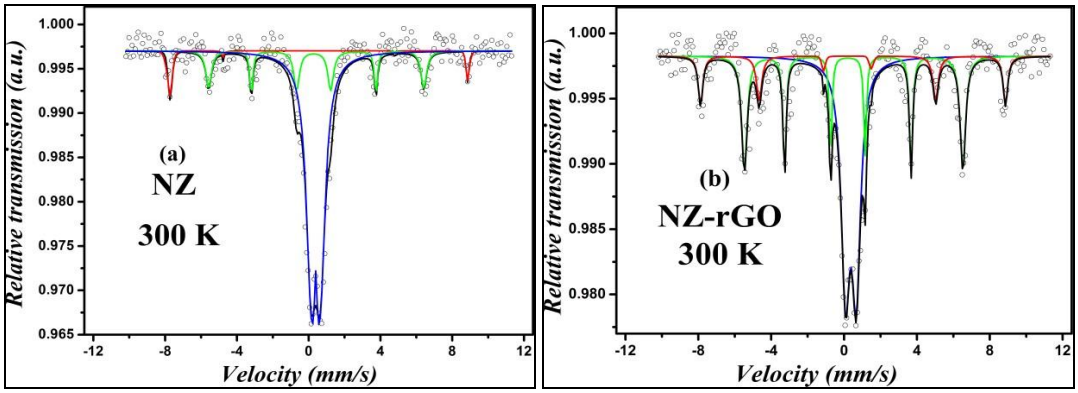

Fig 6: The At room temperature, the Mossbauer spectra of NZ and NZ/rGO are shown in (a) and (b).

A collection of experimental data that includes a pair of and two sextets was used to fit the NZ and NZ/rGO samples. According to references, the centre that Due to the doublet in the NZ Mössbauer spectra, the fraction of nanoparticles with low anisotropy relaxes superparamagmatically. Our previous study has already shown that the value of the doublet's isomer shift has gone up from 0.33 to 0.40 after composite creation. The samples' two ordered magnetic sites are shown by the Zeeman split has two six-finger layouts. According to One sextet is linked to Fe3+ ions at the tetrahedral A site, and the other to the octahedral B site. In addition, since the NZ nanoparticles are dispersed from 0.84 (NZ) to 0.59 (NZ/rGO), the quadrupole splitting (Q.S.) value for the doublet decreases within the rGO matrix. Given that Q.S. is so close to zero is evidence that the sample is practically cubic symmetrical. Analysis shows that after composite creation, Down from 525 KOe, Hint's worth fell to 516 KOe. Metal ion charge-transfer interactions at the interface between ferrite and rGO may be responsible for this decrease. The aforementioned finding may also be attributable to the fact that composite production increases average particle size.

Table 2: Boiling point Mössbauer properties of the specimens.

Sample Temperature Name	Type of Fitting	I.S.[a](mm/s)	Q.S.[b] (mm/s)	L.W.[c] (mm/s)	Hint[d] (K)	% area
	Doublet	0.33	0.84	0.67	-	20.10
NZ 300	Sextet	0.43	0.84	0.67	525.31	34.60
	Sextet	0.40	0.12	0.65	372.70	45.30
	Doublet	0.40	0.59	0.92	-	54.20
NZ/aQ 300	Sextet	0.40	0.10	0.56	516.27	15.10
	Sextet	0.39	0.11	0.55	372.78	30.70

[a] I. S. = Isomer shift,
[b] Q. S. = Quadrupole splitting,
[c] L. W. = Line width,
[d] Hint = Internal hyperfine field

Magnetic property

Figures 7 (a) and (b) present the The M-H loop of NZ and NZ/rGO were measured across a broad field range of 5 Tesla at 300 K and 10 K, respectively, before and after the experiment., using the SQUID magnetometer. Table 2 displays derived from the M-H loops magnetic parameters. An external magnetic field causes the magnetisation to grow until saturation, as seen in Figure 8 (a) and (b). Saturation magnetisation (Ms) values of 48 emu/gm for NZ and 42 emu/gm for NZ/rGO at room temperature demonstrate high ferromagnetism in both samples. The idea of surface moment quenching, which leads to a decrease in saturation magnetisation value, provides an explanation for this behaviour. The formula for the magnetic properties of nanocomposites is According to references, the formula MS= ΦmS is used to calculate the saturation moment for one nanoparticle, and Φ is the proportion of magnetic nanoparticles by volume. Effects of indirect exchange coupling of the Ruderman-Kittel-Kasuya-Yosida type on the magnetic parameters of the hematite-rGO system is thoroughly described in our earlier work. This coupling occurs between the magnetic nanoparticles and isolated rGO spins that are generated by the conduction electrons of rGO. This coupling is in comparison to pure haematite. The coercivity of pure NZ, which was 72 Oe at room temperature before integration into the rGO matrix, rose dramatically to 90 Oe in the current study. Several intrinsic (distribution of metal cations and anions) and extrinsic (crystallite size, nanoparticle density, shape) characteristics may control this improvement. The addition of graphene to ferrite alters the surface morphology, crystal strain, and octahedral and tetrahedral distribution of metal cations, as previously described in the literature. One key component in improving coercivity is increasing the nanocomposite's particle size. For this purpose, you may look at the TEM pictures of NZ and NZ/rGO in Figure 7, 8(a) and (e) for reference. The rGO matrix largely coats the NZ nanoparticles, and they are well-decorated. Adding rGO improves coercivity, which means it increases surface spin-disorder.

In this article, we detail how samples' magnetic properties change when exposed to low temperatures. In most cases, Heat energy gets in the way of magnetic moment alignment. Reducing temperature mitigates the impact of thermal energy, paving the way for an increase in magnetisation. The uncompensated spins located on the nanoparticle surfaces freeze, causing this. When compared to values measured at room temperature, the coercivity value is much greater at 10 K. One possible explanation is that single-domain SPM nanoparticles are being blocked.

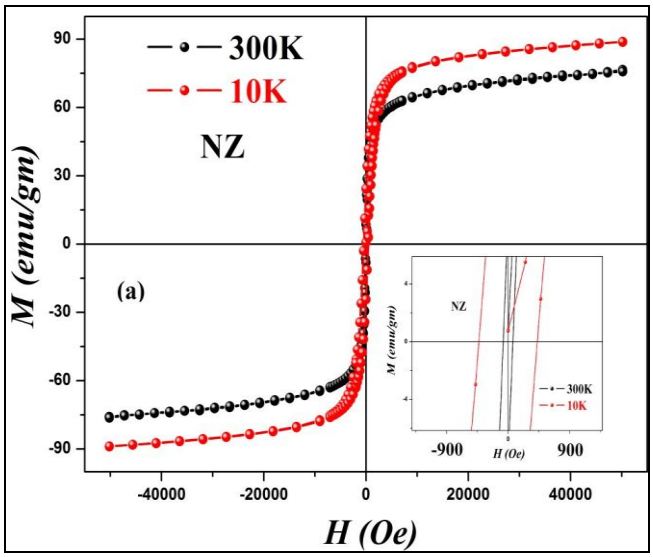

Fig 7: Both the 300 and 10 K measurements of NZ's M-H loops.

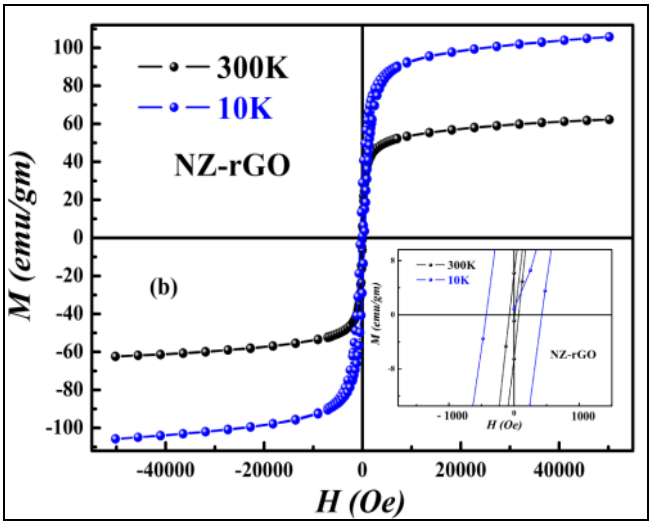

Fig 8: (b) Both 300 K and 10 K were used to capture the M-H cycle of NZ/rGO.

Table 3: Hysteresis loops played back at 10 K and 300 K were used to obtain magnetic properties.

Sample Name	Temperature (K)	Saturation magnetization (MS) (emu/gm)	Coercivity (HC) (Oe)	Remanent magnetization (MR) (emu/gm)
NZ	300	48	72	27
	10	66	395	45
NZ/rGO	300	42	90	38
	10	75	275	49

Conclusion

The study of fingernail clippings using X-ray diffractometry, scanning electron microscopy (SEM), and raman spectroscopy revealed that psoriasis partially destroys the α-helix structure of keratin. Keratin conformational variations affect the surface morphology of healthy nails, affecting uniformity, density, and roughness. The absence of the SH group-inducing peak in psoriasis spectra suggests that psoriasis is more aggressive than onychomycosis, acting on the S-S bond by forming sulfonic groups. Biological therapy also results in -S-S-bridge reformation. The findings suggest that current methodologies for morphological and structural characterization could be used to create reliable and noninvasive dermatologic diagnostic tools.

References

1. Fadia S, Saviska I, Nawawi D, Ismail R, Prihatini E, Laksono G, Wahyuningtyas I. Magnetic characteristics of sengon wood-impregnated magnetite nanoparticles synthesized by the co-precipitation method. AIMS Materials Science. 2024;11:1-27. DOI: 10.3934/matersci.2024001.
2. Trifoi A, Matei E, Râpă M, Banu I, Doukeh R. Coprecipitation nanoarchitectonics for the synthesis of magnetite: a review of mechanism and characterization. Reaction Kinetics, Mechanisms and Catalysis. 2023;136:39. DOI: 10.1007/s11144-023-02514-9.
3. Devi S, Nivetha A, Inbaraj P. Superparamagnetic properties and significant applications of iron oxide nanoparticles for astonishing efficacy-a review. Journal of Superconductivity and Novel Magnetism. 2019;32. DOI: 10.1007/s10948-018-4929-8.
4. Zaman M, Karal M, Khan M, Tareq AR, Ahammed S, Akter M, Hossain A, Ullah A. Eco-friendly synthesis of Fe3O4 nanoparticles based on natural stabilizers and their antibacterial applications. ChemistrySelect. 2019;4. DOI: 10.1002/slct.201901594.
5. Ahadpour Shal A, Jafari A. Study of structural and magnetic properties of superparamagnetic Fe3O4-ZnO core-shell nanoparticles. Journal of Superconductivity and Novel Magnetism. 2013. DOI: 10.1007/s10948-013-2469-9.
6. Moeni M, Edokali M, Rogers M, *et al*. Effect of reaction and post-treatment conditions on physico-chemical properties of magnetic iron oxide nanoparticles. Particuology. 2024;91:155-167. ISSN 1674-2001.
7. Kumar M, Rany M, Ansari JR. Chemical methods for producing iron oxide magnetic nanoparticles: a review. 2024.
8. Hussein M, Samuri S, Shaari A. The effect of synthesis method on the physico-chemical properties of magnetite iron oxide nanoparticles. Advanced Materials Research. 2013;701:212-216. DOI: 10.4028/www.scientific.net/AMR.701.212.
9. Yousif N, Aljawad S, Taha A, Stamatis H. A review of structure, properties, and chemical synthesis of magnetite nanoparticles. Journal of Applied Sciences and Nanotechnology. 2023;3:18-31. DOI: 10.53293/jasn.2022.5179.1178.
10. Khan N, Jameel N. Magnetic nanoparticles-Synthesis, properties and potential applications. 2023;3.
11. Korsakova A, Kotsikau D, Haiduk Y, Pankov V. Synthesis and physicochemical properties of MnxFe3–xO4 solid solutions. Kondensirovannye Sredy i Mezhfaznye Granitsy = Condensed Matter and Interphases. 2020;22:466-472. DOI: 10.17308/kcmf.2020.22/3076.